Soft Matter

PAPER

View Article Online
View Journal | View Issue

Cite this: *Soft Matter*, 2018, **14**, 8051

3D printing of complex origami assemblages for reconfigurable structures†

Zeang Zhao,[ab] Xiao Kuang,[a] Jiangtao Wu,[a] Qiang Zhang,[b] Glaucio H. Paulino,*[c] H. Jerry Qi *[a] and Daining Fang*[bd]

Received 30th June 2018,
Accepted 17th September 2018

DOI: 10.1039/c8sm01341a

rsc.li/soft-matter-journal

Origami engineering principles have recently been applied to a wide range of applications, including soft robots, stretchable electronics, and mechanical metamaterials. In order to achieve the 3D nature of engineered structures (*e.g.* load-bearing capacity) and capture the desired kinematics (*e.g.*, foldability), many origami-inspired engineering designs are assembled from smaller parts and often require binding agents or additional elements for connection. Attempts at direct fabrication of 3D origami structures have been limited by available fabrication technologies and materials. Here, we propose a new method to directly 3D print origami assemblages (that mimic the behavior of their paper counterparts) with acceptable strength and load-bearing capacity for engineering applications. Our approach introduces hinge-panel elements, where the hinge regions are designed with finite thickness and length. The geometrical design of these hinge-panels, informed by both experimental and theoretical analysis, provides the desired mechanical behavior. In order to ensure foldability and repeatability, a novel photocurable elastomer system is developed and the designs are fabricated using digital light processing-based 3D printing technology. Various origami assemblages are produced to demonstrate the design flexibility and fabrication efficiency offered by our 3D printing method for origami structures with enhanced load bearing capacity and selective deformation modes.

1. Introduction

Origami, the traditional art of folding paper, has the potential to inform the design of novel engineered structures. In addition to unique intrinsic properties possessed by some origami tessellations (*e.g.*, negative Poisson's ratio, spatial expandability[1,2]), other properties such as tunable thermal expansion,[3] programmable stiffness,[4] spatial curvature,[5] and multistability,[6] can be introduced through geometrical and material variations. These distinct properties of origami lead to a wide range of potential applications, including soft robots,[7] stretchable electronics,[8,9] metamaterials,[10,11] and optical devices.[12]

Inspired by the field of origami engineering, unit cells of origami tessellations have been repeated in multiple directions in order to fill a predetermined space and fulfill the requirements of load-bearing capacity, stability, and foldability. The simplest method consists of stacking an origami tessellation in a single direction;[2,13,14] but, in this case, design freedom is restricted because stacking is only applicable to some 2D periodic origami systems such as the Miura-ori. Recently, other cellular origami structures were developed by repeating the unit cells in different directions and assembling them into 3D shapes.[15,16] One such design is the tube unit cell composed of two Miura unit cells (Fig. 1A). The tube unit cell is geometrically simple and, when repeated in an aligned[17] or zipper[18] fashion (Fig. 1B), can conform to various 3D contours.[18–21] The zipper coupled tubes have outstanding mechanical behavior, in which load-bearing capacity and expandability can be realized at the same time.[18,20]

Most origami designs have been fabricated by assembling thin sheets made from either paper,[18] plastic,[22] or metal[14] into 3D origami structures, leading to a tedious process and often requiring additional binders or connection elements.[23,24] Recent research has also demonstrated that self-folding[25,26]

[a] *The George W. Woodruff School of Mechanical Engineering, Georgia Institute of Technology, Atlanta, GA 30332, USA. E-mail: qih@me.gatech.edu*
[b] *State Key Laboratory for Turbulence and Complex Systems, College of Engineering, Peking University, Beijing, 100871, P. R. China. E-mail: fangdn@pku.edu.cn*
[c] *School of Civil and Environmental Engineering, Georgia Institute of Technology, Atlanta, GA 30332, USA. E-mail: paulino@gatech.edu*
[d] *Institute of Advanced Structure Technology, Beijing Institute of Technology, Beijing, 100081, P. R. China. E-mail: fangdn@bit.edu.cn*

† Electronic supplementary information (ESI) available: Properties of the photocurable elastomer; derivation of the nonlinear beam (NB) theory; the assembly method of two adjacent origami tubes; the mechanical reliability of the hinge-panel element; geometry parameters of 3D printed origami assemblages; repeatability of the printed origami assemblages; additional information of the printed origami assemblages (PDF). Folding process of the aligned origami tubes and the zipper-coupled origami tubes (MP4). Load-bearing capacity of the aligned origami bridge and the zipper-coupled origami bridge (MP4). Folding process of the square/hexagon coupled origami assemblages (MP4). See DOI: 10.1039/c8sm01341a

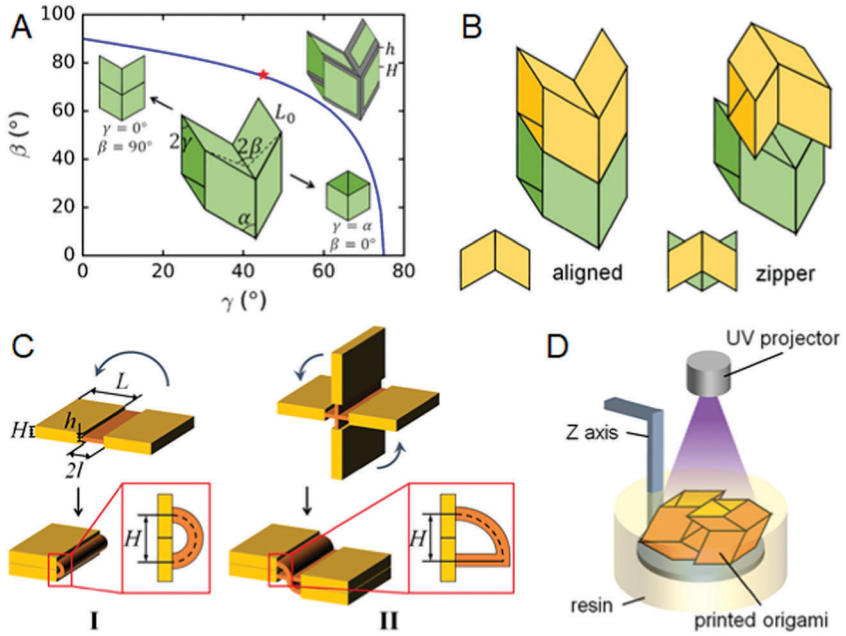

Fig. 1 (A) Geometry of the origami tube unit (variation of the half dihedral angle β through the folding process; the initial half dihedral angle β_0 for the 3D printed origami tubes is marked by the red star). (B) A schematic illustration of the aligned tubes and zipper-coupled origami tubes. (C) The geometry of thick origami hinges. (D) A schematic figure for the DLP 3D printer.

techniques can be used to automatically deploy 3D origami structures from 2D elements. However, the complexity of most self-folding origami structures has not reached the level demonstrated by origami tubes. Direct fabrication of 3D origami assemblages remains challenging.

3D printing is an emerging technology that can be used to directly fabricate complex geometries.[8,27–29] Instead of following the classical fabrication processes including molding, machining, and assembling, these steps are simplified to a single process that greatly enhances design freedom. For direct fabrication of 3D origami structures, extrusion-based 3D printing is undesirable because it is relatively difficult to create parts with meticulous hollow features.[8,27] In addition, the mechanical behavior of printed materials does not resemble that of paper sheets, which can be folded numerous times without severe damage. An alternative method is to use multi-material 3D printing[16,30] to deposit soft materials at the creases and stiff materials at the flat panels, but the complex hollow geometry makes it difficult to remove the sacrificial material, which is necessary for many multi-material 3D printers, such as inkjet 3D printers.

Digital Light Processing (DLP) is an ideal 3D printing technique for fabrication of complex 3D shapes that contain small or hollow features[28,29] because most parts do not require support material (or require less) during the printing process. However, the mechanical performance of most DLP 3D printed materials cannot withstand repeated folding and unfolding, which is typically required in origami-inspired structures.

In this paper, we propose a new method for direct DLP 3D printing of thick origami structures. Limitations in previous 3D printing methods are overcome through a combination of structural design and significantly improved material properties. First, in order to accommodate the folding of thick panels, infinitely narrow creases in paper folding are scaled-up to smooth hinges with finite length (Fig. 1A; the smooth hinges are marked as grey color in the figure), which can be used for complex 3D origami structures, for example, the origami tube assemblages in Fig. 1B. The length l of the hinge is designed for foldability and geometrical compatibility at the same time. Second, the thickness of the hinge is reduced to decrease the folding stiffness (Fig. 1C). The thickness h of the hinge is chosen to ensure the foldability and printing reliability. Finally, the origami structures are printed using a DLP 3D printer with a new photocurable elastomer resin (Fig. 1D) that can accommodate large deformation while being reliable and photocurable at room temperature. Theoretical analyses using a nonlinear beam model and finite element simulations are conducted to improve the design of 3D thick origami assemblages. Origami structures fabricated by this method can easily be folded and expanded. The thick panels also provide the desired load-bearing capacity that moves origami a step closer to actual load-bearing structures. In addition, the programmed deformation mode and anisotropic stiffness of the structure are realized through the geometrical design of the assemblage.

2. Materials and methods

2.1. Photocurable elastomer

To make the photocurable resin, 50 wt% commercial aliphatic urethane diacrylate Ebecryl 8807 was mixed with 25 wt% GMA (glycidyl methacrylate) monomer and 25 wt% IA (isodecyl acrylate)

monomer. 1 wt% Irgacure 819 (phenylbis(2,4,6-trimethylbenzoyl) phosphine oxide) and 0.1 wt% Sudan I was added into the mixture as photoinitiator and photoabsorber, respectively. Ebercryl 8807 was donated by Allnex (Alpharetta, GA, USA). Other chemicals were purchased from Sigma-Aldrich (St. Louis, MO, USA). The viscosity of the resin is low enough for DLP 3D printers without heating up. Tension test and thermomechanical test of the material were implemented on a dynamic mechanical analyzer (DMA, Model Q800, TA Instruments Inc., New Castle, DE, USA). After being fully cured under UV light, the material can be stretched up to 100% with a failure stress around 4 MPa (Fig. S1A, ESI†).

2.2. DLP 3D printing

The DLP 3D printer consists of a UV projector (PRO4500, Wintech Digital Systems Technology Corp., Carlsbad, CA, USA) and a motorized motion stage (MTS50-Z8, Thorlabs Inc., Newton, NJ, USA). Similar to conventional DLP printers, a build platform was attached to the vertically mounted motion stage.[28,29] A set of Matlab (MathWorks, Natick, MA, USA) code was used to control the printing process. The 3D CAD model was sliced to individual grayscale figures by CreationWorkshop (DataTree3D, Dallas, TX, USA). Parameters of the CAD models for different samples are listed in the ESI.† During printing, the grayscale figure for each layer was projected to the liquid resin. In general, the irradiation time of each layer was set to 15 s, which ensured the integrity and stability of the printed structure. For a grayscale figure, the projected light intensity of the white color was around 20 mW cm^{-2}, and the intensity decreased monotonically with the grayscale value.[25] After a layer was cured, the build platform moved down to accommodate the growth of height. The layer-by-layer printing could build structures as tall as 2 cm in one hour. After printing, the sample was cleaned with ethanol and post-cured overnight under UV light.

2.3. Mechanical test

Compression test of the sample was implemented using an electromechanical universal material test machine (MTS Criterion Series 40, Eden Prairie, MN, USA). Different folding configurations of the origami assemblages were exhibited by compressing the structures with a transparent glass slide, and a digital camera (ILCE-6000, Sony Inc., Japan) was utilized to record the deformation.

2.4. Analytical model

To determine the dimensions of the thick origami structures, we describe the hinge-panel element using nonlinear beam (NB) theory.[31,32] Due to symmetry, only one half of the hinge-panel element was considered. The hinge attached to a thick panel in Fig. 2A was simplified to a cantilever beam connected to a rigid bar where the beam represented the hinge and the rigid bar represented the thick panel. The tangential unit vector $\boldsymbol{e}_1$, the normal unit vector $\boldsymbol{e}_2$, and the incline angle θ in the deformed configuration are depicted in Fig. 2A. A linear elastic model was assumed in the theoretical analysis, which was sufficient to describe the deformation under a nominal strain of 20% (Fig. S1A, ESI†):

$$t_1 = EA(\lambda - 1), \tag{1a}$$

$$m = EI\kappa = -EI\frac{\mathrm{d}\theta}{\mathrm{d}S}. \tag{1b}$$

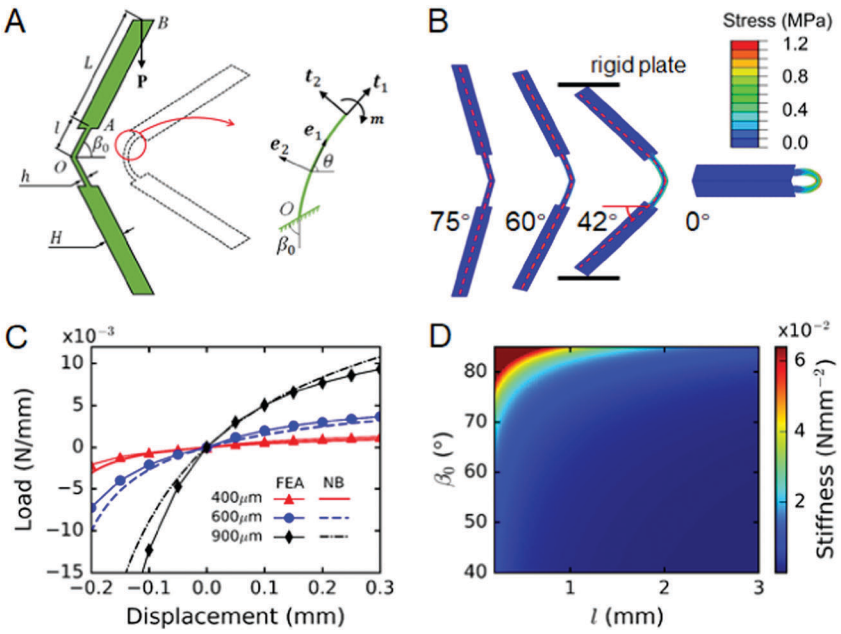

Fig. 2 (A) Schematic figure of the nonlinear beam (NB) model (left: deformation of the hinge together with a rigid panel; right: coordinates definition). (B) Deformation of the hinge and panel at different half dihedral angles β (the contours were calculated by FEA; the dashed lines were calculated by NB). (C) Load (per unit width)-displacement curves of hinges with different thicknesses (FEA and NB). (D) The stiffness (per unit width) of the hinge as a function of hinge length and the initial dihedral angle β_0 (obtained by NB).

Here t_1 is the axial component of the internal force $\boldsymbol{t} = t_1\boldsymbol{e}_1 + t_2\boldsymbol{e}_2$, m is the moment, E = 4 MPa is Young's modulus, λ is the stretch ratio, κ is the curvature of the deformed configuration, S is the local coordinate measured along the axial direction, $A = bh$ is the cross-section area, and $I = bh^3/12$ is the moment of inertia in which b as the width of the beam perpendicular to the plane and h is the thickness of the beam.

The differential equation describing the deformation of the nonlinear beam is,[31]

$$\frac{\mathrm{d}^2\theta}{\mathrm{d}S^2} = -\frac{1}{EI}\left(\frac{t_1}{EA} + 1\right)t_2. \quad (2)$$

The two components of the internal force t_1 and t_2 are related to the initial dihedral angle β_0, the incline angle θ, and the external load P, which remains vertical. Eqn (2) was solved numerically, and the coordinates (x, y) of the beam at the deformed configuration were obtained using the relation $\mathrm{d}x/\mathrm{d}S = \lambda\cos\theta$ and $\mathrm{d}y/\mathrm{d}S = \lambda\sin\theta$. Details of the derivation are provided in the ESI.†

2.5. Finite element simulation

The commercial finite element analysis (FEA) software ABAQUS (Dassault Systemes, Waltham, MA, USA) was used to simulate the deformation of 3D printed structures, and the Arruda–Boyce model[33] was utilized to describe the nonlinear stress–strain relation of the photocurable elastomer (μ = 1.3 MPa, λ_m = 1.7 MPa, obtained by fitting Fig. S1A, ESI†). Two rigid plates, as shown in Fig. 2B, were used to compress the hinge-panel model from the top and the bottom until the hinge-panel was deformed to the fully-folded configuration ($\beta = 0^\circ$). During the FEA simulation, 2D parts were meshed using the plane strain quadrilateral element CPE4R, while 3D parts were meshed using the 8-node linear brick element C3D8R. The flat indenter or rigid plates used in compression experiments were modeled as analytical rigid bodies.

3. Results and discussion

3.1. Photocurable elastomer

A new type of photocurable elastomer was developed to print the 3D origami assemblages (see the Experimental section for details). Without heating up, the liquid resin could be cured under UV light irradiation with fine resolution. The fully cured elastomer can be stretched up to 100% engineering strain (Fig. S1A, ESI†). Following the process in Fig. S1D and E (ESI†), a fully cured elastomer film with a thickness of 0.5 mm was manually folded for around 100 times. After the folding process, we did not observe cracks or crazes on the film. The glass transition temperature of the elastomer is around 15 °C; therefore it is rubbery at room temperature with slight viscoelasticity (Fig. S1B, ESI†).

3.2. Hinge-panel element

We examine the basic design principles that must be applied when thin-sheet origami is extended to 3D printed origami structures. These design principles lead to the "hinge-panel element" depicted in Fig. 1A and C.

In contrast to paper sheets, which can be assumed infinitely thin, the finite thickness and material behavior of 3D printed materials must be taken into consideration for the design of origami-inspired engineering structures. Some general design methods for thick origami have been proposed;[23,24,34] however, those methods focus on single layer origami sheets and typically use a second material at the hinge locations. Here, we aim to design and fabricate 3D origami assemblages that are made of a single material, without assembly of parts. Getting rid of additional binders and connection elements, origami structures can be directly created as a whole, instead of being fabricated step-by-step through cutting, molding, and assembling. The method is applicable to single-layer origami sheets, as well as complex 3D origami structures consisting of several origami units.

In paper folding, microscale damage is caused in the crease region, which permanently reduces the bending stiffness of the crease.[35] In the case of 3D printed elastomers, this type of damage-induced stiffness reduction is detrimental to the reliability of structure. Instead, as in other thick-origami designs, we define a finite-dimensional "hinge" region with reduced stiffness to mimic creases in paper origami. Because we aim to build the entire origami assemblage from a single material, we define a hinge-panel element, consisting of two panels and one hinge (Fig. 2A), in which the hinge has reduced thickness relative to the panels.

The dimensional parameters defined in Fig. 2A are designed so that the assembly of hinge-panels mimics the behavior of the corresponding paper origami assemblage. In the following, we select the panel thickness, H, and panel length, L, to be 1 mm and 6 mm, respectively. Then, we select the hinge thickness, h, hinge length, l, and initial half dihedral angle, β_0, such that we can achieve the desired folding kinematics and such that the stiffness of the hinge allows for the kinematics.

3.3. Comparison of results for the hinge-panel element

In Fig. 2B, we show the deformation of the hinge-panel element based on both the analytical model (dashed red line) and the numerical model with an initial half dihedral angle $\beta_0 = 75^\circ$ (the dihedral angle of the two panels equals to $2\beta_0 = 150^\circ$), hinge thickness h = 0.4 mm, and hinge length, l = 1.6 mm. The deformed shapes and Mises stress fields from the numerical model at different folding angles (or equivalently the half dihedral angle β) are also shown in Fig. 2B. The analysis indicates that during the folding process, high strains and stresses are concentrated in the soft hinge region, while the thick panels remain undeformed during the folding process, leading to relatively small stresses in those regions. The highest stress appears near the center of the hinge but is below the failure stress of the elastomer (Fig. S1A, ESI†). Note that the deformed shape of the hinge-panel element at moderate deformation is captured reasonably well (for example when $\beta = 60^\circ$). The analytical model and the numerical model diverge as the dihedral angle becomes small (for example when $\beta = 42^\circ$).

This discrepancy arises because the linear elastic model might not be accurate enough to describe the mechanics at large strain.

Next, we examine how foldability is affected by changes in the initial half dihedral angle β_0, the hinge length l, and the hinge thickness h. First, h is varied while β_0 and l are held constant (75° and 1.6 mm, respectively). In Fig. 2C, the applied load P is plotted as a function of the vertical displacement at the endpoint B. Here the load is measured per unit width vertical to the paper, and thus the unit of load is N mm^{-1}. Both the analytical results and the simulated results from FEA are nonlinear. As the hinge-panel element is folded ($P \geq 0$), the stiffness of the hinge-panel element decreases. On the contrary, unfolding ($P \leq 0$) the hinge-panel element results in an increase of stiffness, because the element is gradually deformed to the flat shape. As the thickness in the hinge region is reduced (from 900 μm to 400 μm), the slope of the load–displacement curve decreases significantly, indicating an apparent reduction of the folding stiffness. From the results in Fig. 2C, for a flat 1 mm thick panel, reducing the thickness of hinge to 400 μm creates a soft and foldable hinge-panel element.

Subsequently, the thickness of the hinge is held at 400 μm and the length l and the initial dihedral angle β_0 of the hinge are varied in a wide range (from 0 mm to 3 mm, and from 40° to 90°, respectively) to obtain the corresponding load–displacement curves by using the NB model. We define the initial slope of the load–displacement curve as the stiffness, which is plotted as a function of length and initial dihedral angle in Fig. 2D. Here the load is also measured per unit width, and the unit of stiffness is N mm^{-2}. As the value of β_0 approaches 90°, the component of the load P that is perpendicular to the axes of the beam is reduced, causing a significant increase in stiffness. Decreasing the length l of the hinge also results in a stiffer hinge-panel element because it suppresses the rotational deformation at endpoint B, which contributes significantly to the rigid body deformation of the flat panel.

The results in Fig. 2C and D can be summarized as follows: if the thickness h of the hinge is properly reduced, the hinge-panel element only becomes stiff when the initial dihedral angle β_0 is large and the hinge length l is small. Otherwise, changing β_0 and l in a wide range (the deep blue color in Fig. 2D) does not have a significant impact on the stiffness of the hinge-panel.

3.4. Additional design requirements

In addition to stiffness, additional physical requirements need to be considered in designing the hinge-panels. Although the analytical and numerical results indicate that reduced thickness in the hinge region is necessary for reduced stiffness, a finite thickness that depends on the resolution of the DLP 3D printer (typically 50 μm and above) and the stability of the part during printing,[28] is required. If the thickness is too small, the strength of hinge may not be enough to support the whole structure. In our experiments, the thickness of hinge was chosen to be 400 μm, which can ensure printability and foldability at the same time. Printability of the origami structure also influences the choice of the initial half dihedral angle β_0. In the as-printed structures, collapse between adjacent panels should be avoided. During the folding and unfolding process (Fig. 1A), collapse appears in the two extreme conditions as the angle γ changes from 0° to α (while the half dihedral angle β_0 changes from 90° to 0°). As a result, although reducing the half dihedral angle results in reduced hinge stiffness, an intermediate value of 75° (marked by the red star in Fig. 1A) was chosen in our experiments. Additionally, as shown in Fig. 1C-I, if two flat panels connected by a soft hinge are folded together, the length of the hinge must be large enough to accommodate the thickness of panels. Assuming the hinge deforms into a half-circle, the length of the hinge ($2l$) should be more than $\pi H/2$. Following the same discussion, if four flat panels connected by two soft hinges are folded together (Fig. 1C-II), the length ($2l$) of the hinge should be more than πH. Finally, an important design consideration is that a hole should be left at the intersection of adjacent hinges to reduce stress concentrations during folding.

3.5. Design and manufacture of the Miura-ori sheet

As a simple example, we design and manufacture the classical Miura-ori sheet in Fig. 3. The flat panels are printed with a uniform thickness of 1 mm. The 'mountain' and 'valley' creases[1] of the Miura-ori sheet are composed of hinges with a finite length (0.8 mm) and thickness (400 μm according to the previous discussion). The initial dihedral angle is 75°, which ensures foldability. The length of the hinge is determined according to foldability and geometrical compatibility requirements. Assuming the deformed shape of the hinge to be an arc, the length of the hinge is related to the thickness of panels according to $2l = \pi H/2$. Different folding configurations of the printed Miura-ori sheet are shown in Fig. 3B and C. The as-printed sheet can be either folded to the highly compact shape (Fig. 3B), or opened to the flat shape (Fig. 3C).

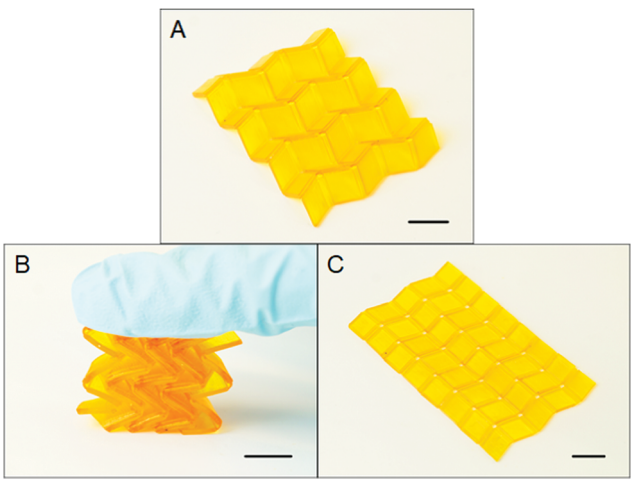

Fig. 3 (A) The as-printed configuration of the Miura-ori sheet. (B) The compact folded configuration of the Miura-ori sheet. (C) The nearly-flat configuration of the Miura-ori sheet. (Scale bar: 5 mm).

3.6. Design and manufacture of the zipper-coupled tube unit cell

Here we are interested in the origami tube unit cell shown in Fig. 1A. Similar to the analysis of a single hinge, the length of the crease on each edge of the origami tube is extended and thinned to reduce the stiffness. As shown in Fig. 1C-II, if the idea of the hinge-panel element is extended to 3D origami assemblages, there will be many interconnections of hinges. In order to fold two adjacent hinge-panel elements at the same time, the length of the hinge should be related to the thickness of panels according to $l = \pi H/2$. During folding of an origami tube (Fig. 1A), the angle γ increases from 0° to α (which is the oblique angle of the flat panel), while the dihedral angle β decreases from 90° to 0°. In our design, an intermediate value of $\gamma = 45°$ was chosen for the as-printed origami tube, and β is related to γ by means of the trigonometric relation $\cos\beta = \tan\gamma/\tan\alpha$. This choice facilitates the printing process, and the dihedral angles of different hinges on the tube will not be too large, which can fulfill the requirement of hinge stiffness (Fig. 2D).

The CAD model of two origami tubes zipper-coupled together is shown in Fig. 4A with finite-dimensional hinges and voids at the intersections of the hinges to facilitate the folding process.[25] The connection faces of the two tubes were cut by half and assembled with each other. As a result, the connection panel between the two tubes possesses the same thickness relative to other panels. The process is shown schematically in Fig. S2 (ESI†). Several 3D printed samples with distinct hinge thicknesses are illustrated in Fig. 4A.

The mechanical properties of the samples were tested by compressing along the central axes of tubes (Fig. 4B). The nonlinear load–displacement relation, similar to that of a single hinge (Fig. 4C), was captured by the FEA simulation. Details of the folding process from the FEA simulation are shown in Fig. 4D. Throughout the folding from the as-printed configuration to the flat configuration, most of the stress is concentrated in the soft hinges. Stresses on the thick flat panel are trivial, and the panel maintains its initial shape throughout the deformation. In addition, the maximum stress in the structure is well below the maximum stress of the material (which is around 4 MPa, Fig. S1A, ESI†).

3.7. Design and manufacture of the large-scale origami assemblages

Next, we apply the design principles to large-scale origami assemblages. As illustrated in Fig. 1C, separate origami tubes can be assembled together in two different manners. In the first case, tubes are assembled along the same direction, and adjacent faces coincide to form 'aligned origami tubes'. In the second case, one set of the tubes is rotated by 180°, and adjacent tubes are assembled in a zig-zag manner, to form the aforementioned 'zipper-coupled origami tubes'.[20] It is noted that in paper origami, these two sets of origami tubes are fabricated separately then glued together; in our DLP 3D printing approach, the assemblages are printed directly without an assembling process, which is a significant advantage of using 3D printing to create origami structures.

A design procedure similar to that for coupling two origami tubes is used to create large-scale origami assemblages. Two types of 3D printed assemblages are shown in Fig. 5. Each of the assemblages consists of 9 tubes, and each tube consists of 4 sections. The coordinate system of the assemblages is defined

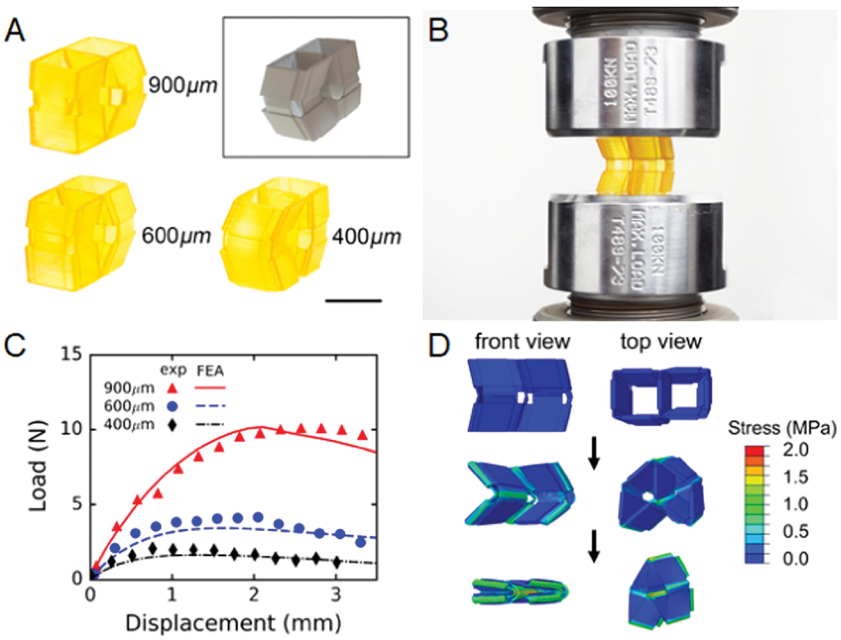

Fig. 4 (A) 3D printed zipper-coupled origami tubes with different hinge thicknesses. (Scale bar: 5 mm; the CAD model is inserted to the right). (B) Experimental setup for the compression of the origami tubes. (C) Load–displacement curves of the zipper coupled origami tubes under compression. (D) FEA simulation of the folding process of the zipper-coupled origami tubes.

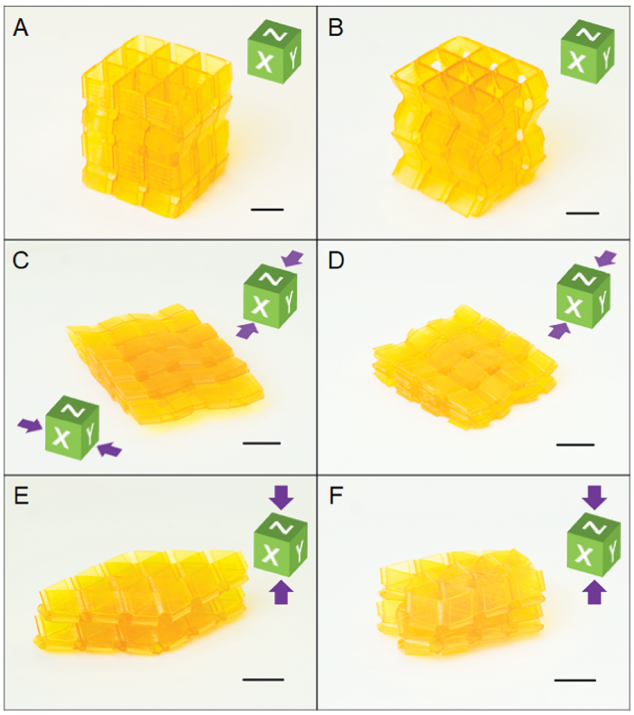

Fig. 5 (A) The as-printed configuration of aligned origami tubes. (B) The as-printed configuration of zipper-coupled origami tubes. (C) Folded configuration of the aligned origami tubes (along direction *X* or *Y*). (D) Folded configuration of the zipper-coupled origami tubes (along direction *X*). (E) Folded configuration of the aligned origami tubes (along direction *Z*). (F) Folded configuration of the zipper-coupled origami tubes (along direction *Z*). (Scale bar: 5 mm).

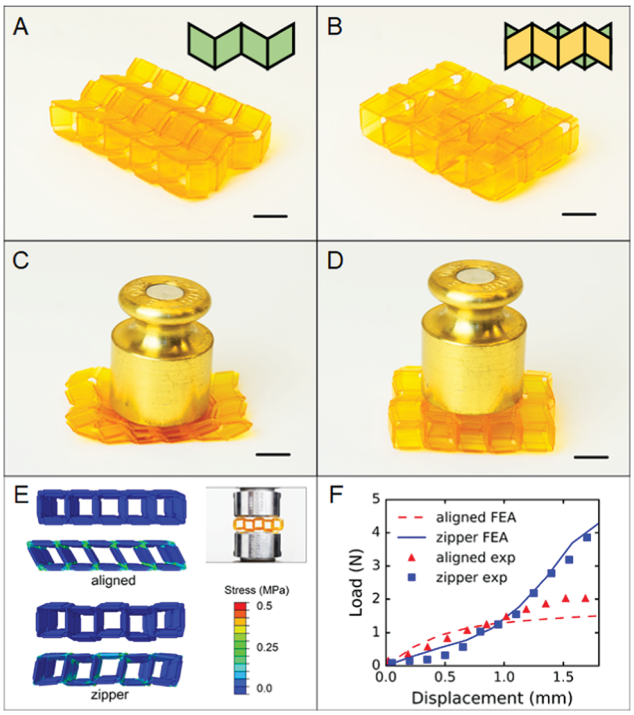

Fig. 6 (A) The as-printed configuration of the "aligned origami" bridge. (B) The as-printed configuration of the "zipper-coupled origami" bridge. (C) The deformed shape of the aligned origami bridge under dead weight. (D) The deformed shape of the zipper-coupled origami bridge under dead weight. (E) FEA simulations of the origami bridges under compression. (F) Load–displacement curves of the origami bridges under compression. (Scale bar: 5 mm; dead weight: 200 g; the weight of the bridge: 2 g).

on the green cubes in Fig. 5. The two as-printed origami assemblages (Fig. 5A and B) created by the two respective methods can be folded into different configurations. When compressed along the *X*-direction or the *Y*-direction, which are symmetrical, the aligned origami tube assemblage is folded into a flat sheet (Fig. 5C). However, a more compact configuration is realized by folding the assemblage along the *Z*-direction (Fig. 5E). The zipper-coupled origami tube assemblage can only be folded by compression along *X*-direction (Fig. 5D) or the *Z*-direction (Fig. 5F), the foldability along the *Y*-direction is restricted by the obstruction between adjacent tubes. The folding process of these two structures is shown in Movie S1 (ESI†). It should be noted that compared with folded aligned origami tubes, the folded zipper-coupled origami tubes are more compact, which is beneficial for use as expandable structures.

A major advantage of zipper-coupled origami tubes is the ability to achieve foldability and load-carrying capability at the same time. Origami bridges fabricated using two types of assembly methods are shown in Fig. 6. Six origami tubes are aligned in parallel to create the bridge in Fig. 6A, and six origami tubes are zipper-coupled to create the bridge in Fig. 6B. When a dead weight of 200 g (which is almost 100 times the weight of the bridge) is put on the top face of the bridge, the aligned origami bridge collapses and folds towards the flat configuration (Fig. 6C and Movie S2, ESI†). However, the zipper-coupled bridge can hold the dead weight and maintain its shape under the load (Fig. 6D) because, similarly to the results in Fig. 5, the foldability of zipper-coupled origami tubes along the vertical direction is restricted by the obstruction between adjacent tubes.

The load-bearing capacity of the zipper-coupled bridge was further confirmed using an FEA simulation. The aligned origami bridge collapsed under compression, as the loading direction coincides with the direction of folding. Under the same compression load, the zipper-coupled bridge only exhibited local stress concentrations (Fig. 6E and F).

In addition to the cellular origami assemblages displayed above, origami tubes can also be assembled into other complex structures. In previous work, many of these structures could only be realized through the folding and gluing of papers.[20,36] In Fig. 7A–D, the six-sided polygonal tubes are assembled with the four-sided quadrilateral tubes. The assembled cross sections are shown on the top of Fig. 7A and C. Two types of assemblages are realized by adjusting the oblique of the tubes along the two different symmetry axes. Due to the geometrical restriction of the hexagon tubes, the square-hexagon coupled assemblage only has one possible folded configuration. The origami assemblage inclined along the long axes of the cross-section could be folded to a flat sheet (Fig. 7A and B), while the origami assemblage inclined along the short axes is folded to a slim shape (Fig. 7C and D). The folding process of the structures in Fig. 7A and C is shown in Movie S3 (ESI†). Fig. 7E and F show

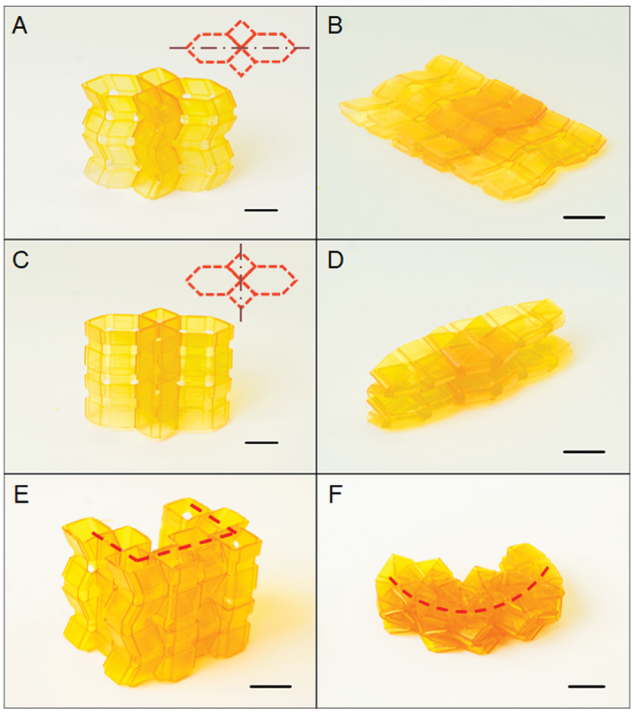

Fig. 7 (A) The as-printed configuration of the mode I square-hexagon coupled assemblage. (B) The deformed shape of the mode I square-hexagon coupled assemblage. (C) The as-printed configuration of the mode II square-hexagon coupled assemblage. (D) The deformed shape of the mode II square-hexagon coupled assemblage. (E) The as-printed configuration of the 'C' shape origami assemblage. (F) The deformed shape of the 'C' shape origami assemblage. (Scale bar: 5 mm).

an example of an adjustable profile curvature in 3D origami assemblages. In Fig. 7E, the square origami tubes are one-by-one zipper assembled to a 'C' shape, with two sharp corners. As we fold the assemblage from the top, the zipper-coupled tubes contract together and the profile became a smooth 'C' shape. The sharp corners are hidden inside the folded panels.

4. Conclusion

In this paper, we propose a new method to directly fabricate 3D origami assemblages out of a single polymeric material using DLP 3D printing technology, without the need to assemble multiple parts. In order to construct origami-inspired structures out of engineering materials, we introduce a hinge-panel element consisting of thick panels and reduced-thickness hinge regions with finite length and thickness. Design parameters of the hinge-panel element, including the thickness, the length, and the dihedral angle, are investigated theoretically and experimentally. By decreasing the thickness of hinges, significant stiffness reduction is created, and folding behavior similar to folding paper is realized. The hinge-panel element is applied to print different 3D origami assemblages that had only been fabricated using paper previously. A novel elastomer system that is photocurable and printable at room temperature is proposed, which ensures the mechanical reliability of 3D printed origami structures. Spatial expandability, load-bearing capacity, and curvature transformation are realized using our geometrical design and assembly methods. This work provides an exploration into the implementation of origami art by engineering materials to engineering structures. The design principles proposed in this work can potentially be extended to other material systems and fabrication methods.

Conflicts of interest

There are no conflicts to declare.

Acknowledgements

We gratefully acknowledge support from an AFOSR grant (FA9550-16-1-0169; Dr B.-L. "Les" Lee, Program Manager); from NSF awards CMMI-1462894, CMMI-1462895, and CMMI-1538830; and from a gift fund from HP. In addition, ZZ, QZ and DF acknowledge support from the National Natural Science Foundation of China (11521202) and from the National Materials Genome Project of China (2016YFB0700600). ZZ also acknowledges support from China Scholarship Council No. 201506010219. GHP acknowledges support from the Raymond Allen Jones Chair at the Georgia Institute of Technology. We appreciate the useful comments provided by Emily D. Sanders.

References

1 Z. Y. Wei, Z. V. Guo, L. Dudte, H. Y. Liang and L. Mahadevan, Geometric Mechanics of Periodic Pleated Origami, *Phys. Rev. Lett.*, 2013, **110**(21), 215501.
2 M. Schenk and S. D. Guest, Geometry of Miura-folded metamaterials, *Proc. Natl. Acad. Sci. U. S. A.*, 2013, **110**(9), 3276–3281.
3 E. Boatti, N. Vasios and K. Bertoldi, Origami Metamaterials for Tunable Thermal Expansion, *Adv. Mater.*, 2017, **29**(26), 1700360.
4 J. L. Silverberg, A. A. Evans, L. McLeod, R. C. Hayward, T. Hull, C. D. Santangelo and I. Cohen, Using origami design principles to fold reprogrammable mechanical metamaterials, *Science*, 2014, **345**(6197), 647–650.
5 L. H. Dudte, E. Vouga, T. Tachi and L. Mahadevan, Programming curvature using origami tessellations, *Nat. Mater.*, 2016, **15**(5), 583–588.
6 B. G. G. Chen, B. Liu, A. A. Evans, J. Paulose, I. Cohen, V. Vitelli and C. D. Santangelo, Topological Mechanics of Origami and Kirigami, *Phys. Rev. Lett.*, 2016, **116**(13), 135501.
7 S. Felton, M. Tolley, E. Demaine, D. Rus and R. Wood, A method for building self-folding machines, *Science*, 2014, **345**(6197), 644–646.
8 Y. H. Zhang, F. Zhang, Z. Yan, Q. Ma, X. L. Li, Y. G. Huang and J. A. Rogers, Printing, folding and assembly methods for forming 3D mesostructures in advanced materials, *Nat. Rev. Mater.*, 2017, **2**(5), 17019.

9 Z. M. Song, T. Ma, R. Tang, Q. Cheng, X. Wang, D. Krishnaraju, R. Panat, C. K. Chan, H. Y. Yu and H. Q. Jiang, Origami lithium-ion batteries, *Nat. Commun.*, 2014, **5**, 3140.

10 Z. Wang, L. Jing, K. Yao, Y. Yang, B. Zheng, C. M. Soukoulis, H. Chen and Y. Liu, Origami-Based Reconfigurable Metamaterials for Tunable Chirality, *Adv. Mater.*, 2017, **29**(27), 1700412.

11 S. Babaee, J. T. B. Overvelde, E. R. Chen, V. Tournat and K. Bertoldi, Reconfigurable origami-inspired acoustic waveguides, *Sci. Adv.*, 2016, **2**(11), e1601019.

12 W. Wang, C. Li, H. Rodrigue, F. P. Yuan, M. W. Han, M. Cho and S. H. Ahn, Kirigami/Origami-Based Soft Deployable Reflector for Optical Beam Steering, *Adv. Funct. Mater.*, 2017, **27**(7), 1604214.

13 X. Zhou, S. X. Zang and Z. You, Origami mechanical metamaterials based on the Miura-derivative fold patterns, *Proc. R. Soc. A*, 2016, **472**(2191), 20160361.

14 J. M. Gattas and Z. You, Geometric assembly of rigid-foldable morphing sandwich structures, *Eng. Struct.*, 2015, **94**, 149–159.

15 N. Yang and J. L. Silverberg, Decoupling local mechanics from large-scale structure in modular metamaterials, *Proc. Natl. Acad. Sci. U. S. A.*, 2017, **114**(14), 3590–3595.

16 K. C. Cheung, T. Tachi, S. Calisch and K. Miura, Origami interleaved tube cellular materials, *Smart Mater. Struct.*, 2014, **23**(9), 094012.

17 T. Tachi and K. Miura, Rigid-foldable cylinders and cells, *J. Int. Assoc. Shell Spat. Struct.*, 2012, **53**, 217–226.

18 E. T. Filipov, T. Tachi and G. H. Paulino, Origami tubes assembled into stiff, yet reconfigurable structures and metamaterials, *Proc. Natl. Acad. Sci. U. S. A.*, 2015, **112**(40), 12321–12326.

19 S. Li, H. Fang and K. W. Wang, Recoverable and Programmable Collapse from Folding Pressurized Origami Cellular Solids, *Phys. Rev. Lett.*, 2016, **117**(11), 114301.

20 E. T. Filipov, G. H. Paulino and T. Tachi, Origami tubes with reconfigurable polygonal cross-sections, *Proc. R. Soc. A*, 2016, **472**(2185), 20150607.

21 H. Yasuda and J. Yang, Reentrant Origami-Based Metamaterials with Negative Poisson's Ratio and Bistability, *Phys. Rev. Lett.*, 2015, **114**(18), 185502.

22 J. T. B. Overvelde, J. C. Weaver, C. Hoberman and K. Bertoldi, Rational design of reconfigurable prismatic architected materials, *Nature*, 2017, **541**(7637), 347–352.

23 Y. Chen, R. Peng and Z. You, Origami of thick panels, *Science*, 2015, **349**(6246), 396–400.

24 S. A. Zirbel, R. J. Lang, M. W. Thomson, D. A. Sigel, P. E. Walkemeyer, B. P. Trease, S. P. Magleby and L. L. Howell, Accommodating Thickness in Origami-Based Deployable Arrays, *J. Mech. Design*, 2013, **135**(11), 111005.

25 Z. Zhao, J. Wu, X. Mu, H. Chen, H. J. Qi and D. Fang, Origami by frontal photopolymerization, *Sci. Adv.*, 2017, **3**, e1602326.

26 T. van Manen, S. Janbaz and A. A. Zadpoor, Programming 2D/3D shape-shifting with hobbyist 3D printers, *Mater. Horiz.*, 2017, **4**(6), 1064–1069.

27 R. L. Truby and J. A. Lewis, Printing soft matter in three dimensions, *Nature*, 2016, **540**(7633), 371–378.

28 J. R. Tumbleston, D. Shirvanyants, N. Ermoshkin, R. Janusziewicz, A. R. Johnson, D. Kelly, K. Chen, R. Pinschmidt, J. P. Rolland, A. Ermoshkin, E. T. Samulski and J. M. DeSimone, Continuous liquid interface production of 3D objects, *Science*, 2015, **347**(6228), 1349–1352.

29 X. Y. Zheng, H. Lee, T. H. Weisgraber, M. Shusteff, J. DeOtte, E. B. Duoss, J. D. Kuntz, M. M. Biener, Q. Ge, J. A. Jackson, S. O. Kucheyev, N. X. Fang and C. M. Spadaccini, Ultralight, Ultrastiff Mechanical Metamaterials, *Science*, 2014, **344**(6190), 1373–1377.

30 Z. Ding, C. Yuan, X. Peng, T. Wang, H. J. Qi and M. L. Dunn, Direct 4D printing via active composite materials, *Sci. Adv.*, 2017, **3**, e1602890.

31 Z. Fan, Y. Zhang, Q. Ma, F. Zhang, H. Fu, K. C. Hwang and Y. Huang, A finite deformation model of planar serpentine interconnects for stretchable electronics, *Int. J. Solids Struct.*, 2016, **91**, 46–54.

32 Y. W. Su, J. Wu, Z. C. Fan, K. C. Hwang, J. Z. Song, Y. G. Huang and J. A. Rogers, Postbuckling analysis and its application to stretchable electronics, *J. Mech. Phys. Solids*, 2012, **60**(3), 487–508.

33 E. M. Arruda and M. C. Boyce, A three-dimensional constitutive model for the large stretch behavior of rubber elastic materials, *J. Mech. Phys. Solids*, 1993, **41**(2), 389–412.

34 R. J. Lang, K. A. Tolman, E. B. Crampton, S. P. Magleby and L. L. Howell, A Review of Thickness-Accommodation Techniques in Origami-Inspired Engineering, *Appl. Mech. Rev.*, 2018, **70**(1), 010805.

35 A. Giampieri, U. Perego and R. Borsari, A constitutive model for the mechanical response of the folding of creased paperboard, *Int. J. Solids Struct.*, 2011, **48**(16–17), 2275–2287.

36 E. T. Filipov, K. Liu, T. Tachi, M. Schenk and G. H. Paulino, Bar and hinge models for scalable analysis of origami, *Int. J. Solids Struct.*, 2017, **124**, 26–45.